



# Thermal shock resistance and failure probability analysis on solid oxide electrolyte direct flame fuel cells



Yuqing Wang, Yixiang Shi\*, Xiankai Yu, Ningsheng Cai

Key Laboratory for Thermal Science and Power Engineering of Ministry of Education, Department of Thermal Engineering, Tsinghua University, Beijing 100084, China

## HIGHLIGHTS

- Thermal shock resistance was analyzed for direct flame fuel cells.
- Mass/charge/heat transport processes and thermal mechanical stress were coupled.
- Effects of cell structures (anode or electrolyte supported SOFC) were studied.
- Effects of flame temperature non-uniformity and heating process were studied.

## ARTICLE INFO

### Article history:

Received 7 June 2013

Received in revised form

27 December 2013

Accepted 8 January 2014

Available online 18 January 2014

### Keywords:

Direct flame fuel cell

Thermal shock resistance

Stress

Failure probability

Flame uniformity

## ABSTRACT

A detailed two-dimensional model of direct flame fuel cell (DFFC) was developed by considering the coupling effects of heterogeneous chemical and electrochemical reactions, electrode microstructure, transport processes of mass, charge and energy, as well as the thermal mechanical stress. The stress distribution was simulated at different heat-up rates which represent the typical DFFC and the common solid oxide fuel cell (SOFC) operation. Transient temperature field and associated thermal stress distributions are determined and analyzed for two different cell structures. The failure probability of the fuel cell is defined and estimated by employing the Weibull statistic. The model is demonstrated to be a useful tool for understanding the mechanical stress distribution within a DFFC cell and for the cell structure design and optimization. The results reveal that the failure probability of an SOFC cell plate working in flame conditions may be 6 orders higher than that in the common SOFC operation conditions. The anode-supported SOFC shows better thermal shock resistance compared with the electrolyte-supported SOFC. The uniformity of the flame temperature is vital in the DFFC system since the non-uniform distribution of the flame temperature greatly increases the failure probability.

© 2014 Elsevier B.V. All rights reserved.

## 1. Introduction

Direct flame fuel cell (DFFC) is a kind of novel fuel cell, which combines the flame and the solid oxide fuel cell (SOFC) in a “no-chamber” setup [1]. The flame consumes the oxygen at the anode side and provides the reacting heat for keeping the SOFC operating temperature. The cathode is exposed to the air to maintain the gas concentration gradient between the different electrodes [1–6]. Compared to the conventional dual-chamber and single-chamber SOFC, DFFC has the advantages in fuel-flexibility, sealing, simple setup and rapid start-up.

Thermal stresses are the main factors for the failure of solid oxide fuel cells, especially for DFFC operation. During the operation of DFFC, the fuel cell plate is heated up much more rapidly by the flame compared to the temperature rising rate in common SOFC operating conditions and this may lead to significant thermal stress to the cell. In addition, the non-uniform temperature distribution of fuel cell generated of common flame can also lead to the variation of fuel cell temperature, which will lead to the thermal stress of SOFC as well. Thus, it is significantly important to analyze the thermal shock resistance and failure possibilities of SOFC for operating in typical flame conditions, which will be crucial for novel DFFC prototype design and performance optimization. Currently, although numerous studies have been carried out on thermal stresses for SOFC experimentally and theoretically, more specific models should be studied in order to quantify and predict the magnitude of the thermal stress in SOFC operating in flame conditions.

\* Corresponding author. Tel./fax: +86 1062789955.

E-mail address: [shyx@tsinghua.edu.cn](mailto:shyx@tsinghua.edu.cn) (Y. Shi).

In this study, a mechanistic model for DFFC by coupling the mass transport processes, the energy conservation, the electrochemistry and the mechanical stress is developed. The thermal shock resistance of the DFFC configuration is studied. Transient temperature field and associated thermal stresses are determined and compared for two DFFC structures which are based on the anode-supported SOFC (ASSOFC) and the electrolyte-supported SOFC (ESSOFC) separately. The influences of the flame non-uniformity on DFFC performance and the stress field are studied. The Weibull statistic is employed to estimate the failure probability of the DFFC during the start-up and operation period.

## 2. Model development

### 2.1. Model geometry

The geometry of the model exhibits a two dimensional (2D) planar type DFFC as seen in Fig. 1. In the DFFC setup, the fuel cell was located above the flame with the anode facing the flame front and the cathode exposed to ambient air. Two different cell structures (ASSOFC and ESSOFC) are studied and the dimensions are given in Table 1. The thicknesses of the cell layers ( $t_a$ ,  $t_e$ ,  $t_c$  in Fig. 1) are chosen as the configurations which are commonly used in published literature [7–9].

### 2.2. Model assumptions

The main assumptions are listed as the following:

- (1) The electrochemical reactions spatially occurred along electrode thickness within the electrode. The reaction active sites are assumed to be uniformly distributed in each electrode layer. The two conducting phases (electronic and ionic) are considered to be continuous and homogeneous in each layer.
- (2) The charge transfer reaction is assumed to take place at the three phase boundary (TPB).
- (3) A mixture of  $H_2$ ,  $CO$ ,  $H_2O$ ,  $CO_2$  gases with a typical flame composition were chosen as the anode gases and the cathode gas was chosen as air. All of the gasses are considered as ideal gases.
- (4) The convection flux and pressure gradient in the porous electrodes are ignored.
- (5) Radiative heat transfer is neglected within the whole cell.
- (6) The temperature load is considered to be the only one in stress analysis.

### 2.3. Governing equations

#### 2.3.1. Charge conservation

The governing equations for SOFC electrode transient charge balance were shown as follows [10,11]:

**Table 1**  
Dimensions of the fuel cells.

	ASSOFC	ESSOFC
$l$	50 mm	50 mm
$t_a$	1000 $\mu\text{m}$	50 $\mu\text{m}$
$t_e$	20 $\mu\text{m}$	150 $\mu\text{m}$
$t_c$	60 $\mu\text{m}$	50 $\mu\text{m}$

Ionic charge balance at the anode:

$$\begin{aligned} & \frac{C_{dl,an} S_{act,an} \partial(V_{ion,an} - V_{el,an})}{\partial t} + \nabla \cdot (-\sigma_{ion,an}^{eff} \nabla V_{ion,an}) = Q_{ion,an} \\ & = - \left( i_{0,an,H_2} \frac{C_{H_2}^{TPB}}{C_{H_2}^{bulk}} + i_{0,an,CO} \frac{C_{CO}^{TPB}}{C_{CO}^{bulk}} \right) \\ & \quad S_{act,an} \left( \exp \left( \frac{\alpha n_e F (V_{el,an} - V_{ion,an} - V_{ref,an})}{RT} \right) \right. \\ & \quad \left. - \exp \left( - \frac{(1-\alpha) n_e F (V_{el,an} - V_{ion,an} - V_{ref,an})}{RT} \right) \right) \end{aligned} \quad (1)$$

Electronic charge balance at the anode:

$$\begin{aligned} & \frac{C_{dl,an} S_{act,an} \partial(V_{el,an} - V_{ion,an})}{\partial t} + \nabla \cdot (-\sigma_{el,an} \nabla V_{el,an}) = Q_{el,an} \\ & = -Q_{ion,an} \end{aligned} \quad (2)$$

Ionic charge balance at the cathode:

$$\begin{aligned} & \frac{C_{dl,ca} S_{act,ca} \partial(V_{ion,ca} - V_{el,ca})}{\partial t} + \nabla \cdot (-\sigma_{ion,ca}^{eff} \nabla V_{ion,ca}) = Q_{ion,ca} \\ & = i_{0,ca} S_{act,ca} \frac{C_{O_2}^{TPB}}{C_{O_2}^{bulk}} \left( \exp \left( \frac{\alpha n_e F (V_{el,ca} - V_{ion,ca} - V_{ref,ca})}{RT} \right) \right. \\ & \quad \left. - \exp \left( - \frac{(1-\alpha) n_e F (V_{el,ca} - V_{ion,ca} - V_{ref,ca})}{RT} \right) \right) \end{aligned} \quad (3)$$

Electronic charge balance at the cathode:

$$\begin{aligned} & \frac{C_{dl,ca} S_{act,ca} \partial(V_{el,ca} - V_{ion,ca})}{\partial t} + \nabla \cdot (-\sigma_{el,ca}^{eff} \nabla V_{el,ca}) = Q_{el,ca} \\ & = -Q_{ion,ca} \end{aligned} \quad (4)$$

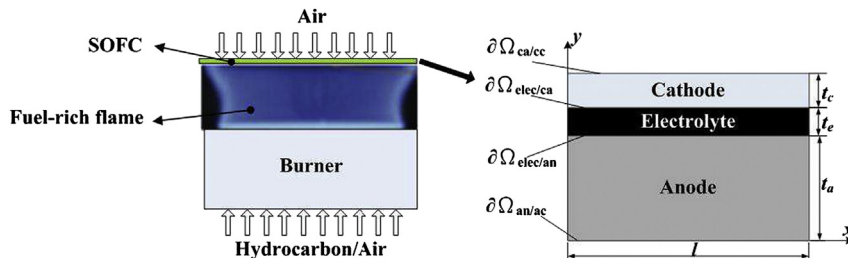


**Fig. 1.** DFFC setup (left) and simplified 2D model geometry of planar SOFC (right).

where  $t$  is time,  $C_{dl}$  is the specific interface double-layer capacitance between electronic and ionic conductor phases;  $Q$  is the transfer current source;  $V_{el}$  and  $V_{ion}$  denote the electric potential of the two conductor phases [10].

### 2.3.2. Chemical reaction model

Reversible water–gas shift reaction (WGSR, Eq. (5)) and reversible direct internal reforming reaction (DIR, Eq. (6)) have been taken into consideration, which is called internal reforming as well.



The above chemical reactions are assumed to be limited in the anode which can provide Ni catalyst. Haberman and Young's model is adopted to describe the rate of reversible WGSR and DIR [12]. The expressions of reversible WGSR rate ( $R_{\text{shift}}$ ,  $\text{mol m}^{-3} \text{ s}^{-1}$ ) and reversible DIR rate ( $R_{\text{reform}}$ ,  $\text{mol m}^{-3} \text{ s}^{-1}$ ) are shown as following.

$$R_{\text{shift}} = k_{\text{sf}} \left( p_{\text{H}_2\text{O}} p_{\text{CO}} - \frac{p_{\text{H}_2} p_{\text{CO}_2}}{K_{\text{ps}}} \right) \quad (7)$$

$$k_{\text{sf}} = 0.0171 \exp\left(\frac{-103191}{RT}\right), \text{mol m}^{-3} \text{ Pa}^{-2} \text{ s}^{-1} \quad (8)$$

$$K_{\text{ps}} = \exp\left(-0.2935Z^3 + 0.6351Z^2 + 4.1788Z + 0.3169\right) \quad (9)$$

$$Z = \frac{1000}{T(K)} - 1 \quad (10)$$

$$R_{\text{reform}} = k_{\text{rf}} \left( p_{\text{CH}_4} p_{\text{H}_2\text{O}} - \frac{p_{\text{H}_2}^3 p_{\text{CO}}}{K_{\text{pr}}} \right) \quad (11)$$

$$k_{\text{rf}} = 2395 \exp\left(\frac{-231266}{RT}\right), \text{mol m}^{-3} \text{ Pa}^{-2} \text{ s}^{-1} \quad (12)$$

$$K_{\text{ps}} = 1.0267 \times 10^{10} \times \exp\left(-0.2513Z^4 + 0.3665Z^3 + 0.5810Z^2 - 27.134Z + 3.277\right) \quad (13)$$

The heat generation/consumption from chemical reaction is considered. The values are given in Table 4.

### 2.3.3. Mass balance

It is generally agreed that one of the most convenient approach for modeling the gas transport in the porous electrode is the dusty-gas model (DGM).

The DGM could be formulated as follows while neglecting the pressure gradient in the porous electrode and the implicit relationship between the species mole fraction and molar diffusion fluxes was provided,

$$-c \nabla x_i = \sum_{j=1, i \neq j}^n \left( \frac{x_j N_i - x_i N_j}{D_{ij}^{\text{eff}}} \right) + \frac{N_i}{D_{\text{kn},i}^{\text{eff}}}, \quad i = 1, 2, 3, \dots, n \quad (14)$$

where, the effective molecular diffusion coefficients  $D_{ij}^{\text{eff}}$  and the effective Knudsen diffusion coefficients  $D_{\text{kn},i}^{\text{eff}}$  can be calculated by considering the porous material property as,

$$D_{ij}^{\text{eff}} = \frac{\varepsilon}{\tau} D_{ij} = \frac{0.00101 T^{1.75} \left( \frac{1}{M_i} + \frac{1}{M_j} \right)^{1/2}}{P \left[ V_i^{1/3} + V_j^{1/3} \right]^2} \quad (15)$$

$$D_{\text{kn},i}^{\text{eff}} = \frac{\varepsilon}{\tau} D_{\text{kn},i} = 97.0 \frac{\varepsilon \bar{r}}{\tau} \sqrt{\frac{T}{M_i}} \quad (16)$$

where,  $\varepsilon$  is the electrode porosity,  $\tau$  is the tortuosity factor,  $V$  is the diffusion volume and  $\bar{r}$  denotes the average pore radius.

Eq. 14 can be formulated as the explicit relationship between species model fractions and molar fluxes using matrix notation, and eventually we can get,

$$\frac{\partial(\varepsilon \rho w_i)}{\partial t} + \nabla \cdot \left( -\rho w_i \sum_{j=1}^n \bar{D}_{ij} \nabla x_j \right) = R_i \quad (17)$$

The equations for electrode mass balances can be summarized as follows (Table 2):

### 2.3.4. Energy conservation

The governing equations for energy balance were shown as follows:

$$\frac{\partial(\rho C_p T)}{\partial t} + \nabla \cdot (-\lambda_{\text{eff}} \nabla T) = Q_{\text{heat}} \quad (18)$$

where  $\lambda_{\text{eff}}$  is the effective thermal conductivity of the porous electrodes,

**Table 2**  
Governing equations for mass conservation.

Domain	Governing equations
Anode	$\frac{\partial(\varepsilon_{\text{an}} \rho_{\text{an}} w_{\text{H}_2\text{O}})}{\partial t} + \nabla \cdot (-\rho_{\text{an}} w_{\text{H}_2\text{O}} \sum_{j=1}^n (\bar{D}_{\text{H}_2\text{O},j} \nabla x_j)) = M_{\text{H}_2\text{O}} \left( \frac{i_{\text{trans,an,H}_2} S_{\text{act,an}}}{2F} - 3R_{\text{reform}} - R_{\text{shift}} \right)$ $\frac{\partial(\varepsilon_{\text{an}} \rho_{\text{an}} w_{\text{H}_2})}{\partial t} + \nabla \cdot (-\rho_{\text{an}} w_{\text{H}_2} \sum_{j=1}^n (\bar{D}_{\text{H}_2,j} \nabla x_j)) = M_{\text{H}_2} \left( 3R_{\text{reform}} + R_{\text{shift}} - \frac{i_{\text{trans,an,H}_2} S_{\text{act,an}}}{2F} \right)$ $\frac{\partial(\varepsilon_{\text{an}} \rho_{\text{an}} w_{\text{CO}_2})}{\partial t} + \nabla \cdot (-\rho_{\text{an}} w_{\text{CO}_2} \sum_{j=1}^n (\bar{D}_{\text{CO}_2,j} \nabla x_j)) = M_{\text{CO}_2} \left( R_{\text{reform}} + R_{\text{shift}} + \frac{i_{\text{trans,an,CO}} S_{\text{act,an}}}{2F} \right)$ $\frac{\partial(\varepsilon_{\text{an}} \rho_{\text{an}} w_{\text{CO}})}{\partial t} + \nabla \cdot (-\rho_{\text{an}} w_{\text{CO}} \sum_{j=1}^n (\bar{D}_{\text{CO},j} \nabla x_j)) = M_{\text{CO}} \left( R_{\text{reform}} - R_{\text{shift}} - \frac{i_{\text{trans,an,CO}} S_{\text{act,an}}}{2F} \right)$
Cathode	$\frac{\partial(\varepsilon_{\text{ca}} \rho_{\text{ca}} w_{\text{O}_2})}{\partial t} + \nabla \cdot (-\rho_{\text{ca}} w_{\text{O}_2} \sum_{j=1}^n (\bar{D}_{\text{O}_2,j} \nabla x_{\text{O}_2})) = \frac{i_{\text{trans,ca,O}_2} S_{\text{act,ca}}}{4F}$

$$\lambda_{\text{eff}} = -2\lambda_s + \frac{1}{\frac{\varepsilon}{2\lambda_s + \lambda_g} + \frac{1-\varepsilon}{3\lambda_s}} \quad (19)$$

where,  $\lambda_s$  and  $\lambda_g$  are thermal conductivities of solid phase and gas phase materials in porous electrodes.  $Q_{\text{heat}}$  is the heat source term, and can be calculated as the following equation in different solid structures,

$$Q_{\text{heat}} = \begin{cases} Q_{\text{ohm}}, \text{electrolyte} \\ Q_{\text{ohm}} + Q_{\text{rev}} + Q_{\text{irr}}, \text{porous electrode} \end{cases} \quad (20)$$

where, the  $Q_{\text{ohm}}$  is the ohmic heat and can be calculated as,

$$Q_{\text{ohm}} = \begin{cases} \frac{i_{\text{ion}}^2}{\sigma_{\text{ion}}}, \text{electrolyte} \\ \frac{i_{\text{ion}}^2}{\sigma_{\text{ion}}} + \frac{i_{\text{el}}^2}{\sigma_{\text{el}}}, \text{porous electrode} \end{cases} \quad (21)$$

where,  $i$  is the local electronic or ionic current density,  $\sigma$  is the electric conductivity.

$Q_{\text{rev}}$  is the reversible heat effects of entropy change in electrochemical reactions, and can be calculated as,

$$Q_{\text{rev}} = \begin{cases} \frac{i_{\text{trans,ca,H}_2\text{O}} S_{\text{act,ca}} T (S_{\text{H}_2\text{O}} + 2S_{\text{e}^-} - S_{\text{H}_2} - S_{\text{O}_2})}{2F} + \frac{i_{\text{trans,ca,CO}_2} S_{\text{act,ca}} T (S_{\text{CO}_2} + 2S_{\text{e}^-} - S_{\text{CO}} - S_{\text{O}_2})}{2F} + R_{\text{shift}} Q_{\text{shift}} + R_{\text{reform}} Q_{\text{reform}}, \text{cathode} \\ \frac{i_{\text{trans,an}} S_{\text{act,an}} T (S_{\text{O}_2} - \frac{1}{2} S_{\text{O}_2} - 2S_{\text{e}^-})}{2F}, \text{anode} \end{cases} \quad (22)$$

where,  $S$  is the molar entropies of species. Then the cathode entropy change can be calculated by subtracting anode entropy change from whole the entropy change of electrochemical reaction.  $Q_{\text{irr}}$  is the irreversible heat generation due to activation polarizations which can be formulated as,

$$Q_{\text{irr}} = |\eta Q_{\text{el}}| = |\eta Q_{\text{ion}}| \quad (23)$$

### 2.3.5. Mechanical model

Thermal stress in the three-layered structure (anode, electrolyte and cathode) was calculated using the solid model within Structural Mechanics Module in the finite element commercial software COMSOL MULTIPHYSICS®. It should be noted that the mechanical model considers only the thermal load and the reference temperature is assumed to be 1283 K following Atkinson and Selcuk [13].

### 2.4. Boundary conditions

The boundaries of the model geometry are labeled in Fig. 1. The detailed settings of boundary conditions for the partial differential equations are listed in Table 3.

The boundary conditions “Insulation” and “Continuity” mean that the partial derivative is zero and the flux is continuous of the

**Table 3**  
Boundary conditions.

Boundary	Ionic charge	Electronic charge	Mass balance	Energy conservation	Mechanical
$\partial\Omega_{\text{an/ac}}$	Insulation	$V_{\text{cell,an}}$	$w_{\text{g,an}}$	$T_{\text{an}}$	Free
$\partial\Omega_{\text{elec/an}}$	Continuity	Insulation	Insulation	Continuity	Continuity
$\partial\Omega_{\text{elec/ca}}$	Continuity	Insulation	Insulation	Continuity	Continuity
$\partial\Omega_{\text{ca/cc}}$	Insulation	$V_{\text{cell,ca}}$	$w_{\text{g,ca}}$	Convective heat flux	Free
Others	Insulation	Insulation	Insulation	Insulation	Free

**Table 4**

Pore structure parameters in the porous electrode [17].

Cell layer	Porosity	Mean pore radius ( $\mu\text{m}$ )	$S_{\text{TPB}}$ ( $\text{m}^2 \text{m}^{-3}$ )	$S_{\text{Ni}}$ ( $\text{m}^2 \text{m}^{-3}$ )
Anode	0.36	0.193	$2.14 \times 10^5$	$3.82 \times 10^6$
Cathode	0.36	0.193	$2.14 \times 10^5$	—

variables at the boundary, respectively.  $w_{\text{g,an}}$  is the mass fraction of the flame species and  $w_{\text{g,ca}}$  is the mass fraction of gas species in the cathode. The difference between  $V_{\text{cell,an}}$  and  $V_{\text{cell,ca}}$  is the cell operation voltage in the calculation, and  $V_{\text{cell,ca}}$  was set as zero.  $T_{\text{an}}$  in the table represents the flame temperature and the convective heat flux boundary means  $n \cdot (-\lambda \nabla T) = 0$ . The mechanical boundary condition “Free” means that the fuel cell is not constrained and free to bend.

### 2.5. Model parameters

#### 2.5.1. Model parameters for the thermo-electrochemical model

In Section 2.3.1 and 2.3.3, the effective reaction area, TPB area and TPB length are needed in the calculation. The parameter  $S_{\text{TPB}}$

can be formulated by using the particle coordination number in binary random packing of spheres together with percolation theory as [14,15]. The physical properties of gas mixture, e.g. specific heat capacity, heat conductivity, viscosity et al. were calculated in the well-correlated equations with temperature in the works of Young et al. [16]. The typical SOFC cell materials (i.e. Ni–YSZ/YSZ/LSM) have been considered for this study. To be more specific, the thermophysical properties of zirconia stabilized with 8% mol of  $\text{Y}_2\text{O}_3$

**Table 5**

Model parameters for the thermo-electrochemical model [11,12,18,19].

Parameters	Value
Electric conductivity ( $\text{S m}^{-1}$ )	
Ionic conductor YSZ, $\sigma_{\text{YSZ}}$	$3.34\text{e}4 \exp(-10,300/T)$
Electronic conductor LSM, $\sigma_{\text{LSM}}$	$4.2\text{e}7/T \exp(-1150/T)$
Electronic conductor Ni, $\sigma_{\text{Ni}}$	$3.27\text{e}6-1065.3T$
Heat conductivity ( $\text{W m}^{-1} \text{K}^{-1}$ )	
Anode, $\lambda_{\text{an}}$	6.23
Cathode, $\lambda_{\text{ca}}$	9.6
Electrolyte, $\lambda_{\text{elec}}$	2.7
Density ( $\text{kg m}^{-3}$ )	
Anode, $\rho_{\text{an}}$	3030
Cathode, $\rho_{\text{ca}}$	3310
Electrolyte, $\rho_{\text{elec}}$	5160
Heat capacity ( $\text{J kg}^{-1} \text{K}^{-1}$ )	
Anode, $C_{\text{p,an}}$	595
Cathode, $C_{\text{p,ca}}$	573
Electrolyte, $C_{\text{p,elec}}$	606
Parameters of chemical reaction	
DIR reaction heat $Q_{\text{reform}}$ , $\text{J mol}^{-1}$	–20,600
WGS reaction heat $Q_{\text{shift}}$ , $\text{J mol}^{-1}$	41,000
Parameters of electrochemical reaction kinetics	
Interface conductivity $\beta_{\text{an}}/\beta_{\text{ca}}$ , $\Omega^{-1} \text{m}^{-2}$	$6.8\text{e}12/5.8\text{e}10$
Activation energy $E_{\text{act,an}}/E_{\text{act,ca}}$ , $\text{J mol}^{-1}$	120,000/130,000
Microstructures	
Anode porosity/tortuosity/pore radius, $\mu\text{m}$	0.36/5/0.193
Cathode porosity/tortuosity/pore radius, $\mu\text{m}$	0.36/3/0.193

**Table 6**  
Elastic properties of each cell material.

	Temp	Anode Ni/YSZ	Electrolyte YSZ	Cathode LSM
$E$ (GPa)	298 K	76.75 [21]	190 [22]	41 [20]
	1073 K	63.4 [21]	157 [22]	43.4 [20]
$\nu$	298 K	0.283 [21]	0.308 [22]	0.28 [20]
	1073 K	0.286 [21]	0.313 [22]	0.28 [20]
$\alpha$ ( $\times 10^{-5}$ )	298 K	11.7 [24]	7.6 [23]	9.8 [23]
	1273 K	12.5 [24]	10.5 [23]	11.8 [23]

(YSZ),  $\text{La}_{0.8}\text{Sr}_{0.2}\text{MnO}_3$  (LSM) and a Ni–YSZ cermet which is reduced from an oxidized form NiO–YSZ (50% wt of NiO) were used in the model, as shown in Table 5. These parameter values were based on the values from published literature and the temperature dependence of the heat conductivity, density and heat capacity of all solid materials were all considered negligible in this model.

### 2.5.2. Thermo-elastic material properties

The elastic modulus and Poisson's ratio of the porous cathode and anode have been shown to be strongly dependent on porosity [20,21]. It should be noted that the porosity of the anode heavily depends on the oxidized or reduced state of the nickel phase and the anode is considered to be in the reduced state with the porosity of 36% in this model. Besides, the thermo-elastic material properties are dependent on the temperature and are summarized in Table 6. A linear interpolation is assumed between the data points quoted from the literature.

### 2.6. Model solution

The calculations were performed using the finite element commercial software COMSOL MULTIPHYSICS®. The symmetry mapping structured quadrilateral mesh was used in the solution. The mesh consists of 7150 and 9750 elements separately for the ASSOFC and ESSOFC. The default stationary nonlinear solver (uses damped Newton method with direct linear system solver UMF-PACK) of COMSOL MULTIPHYSICS® was used to solve the thermo-electrochemical model. The time dependent segregated solver was used to solve the time-dependent thermo-mechanical model.

## 3. Results and discussions

### 3.1. Mechanical model validation

The validity of the proposed thermo-electrochemical model in this paper has been validated in our previous studies [25]. The mechanical part of the model is further validated in this paper. The mechanical model is checked by experimental data and an analytical model developed by Hsueh [26] separately.

#### 3.1.1. Validation by experimental data

In the experiments of Refs. [27] and [28], the residual thermal stresses in the electrolyte layer of a half-cell were measured at

**Table 7**  
Comparison of simulation and experimental residual thermal stresses in the electrolyte layer.

	Temp	Electrolyte thickness ( $\mu\text{m}$ )	Anode thickness ( $\mu\text{m}$ )	Electrolyte residual stress (MPa)
Experiment	298 K	10	510	–300 [27]
Simulation				–384
Experiment	1073 K	10	510	–50 [27]
Simulation				–81
Experiment	298 K	10	1500	–520 [28]
Simulation				–423

different temperatures. In order to validate the mechanical model, the stress fields in the half-cell consisting of a porous Ni/8YSZ anode layer and a dense 8YSZ electrolyte layer were firstly calculated and compared with the experimental data in Table 7. It can be seen that between room temperature and 1073 K a decrease from –300 MPa to –50 MPa of residual thermal stresses has been measured for 10- $\mu\text{m}$  YSZ electrolyte on 510- $\mu\text{m}$  Ni-YSZ anode [27], which is from –384 MPa to –81 MPa in simulation. Fischer et al. [28] reported a compressive thermal stress of 520 MPa for a half-cell with an anode thickness of 1.5 mm and an electrolyte thickness of 10  $\mu\text{m}$ , which is higher than the simulation result 423 MPa. There exists a difference between the measured thermal stress data in experiment and our simulation results, but they are within the same order of magnitude. The difference is possibly due to the difference in anode composition, anode density, and electrolyte density which will influence the Young's modulus of these materials and the thermal stresses. It should be noted that it is difficult to directly compare the experimental data and the simulation results since the exact geometrical parameters and material properties are not available for the stresses reported.

#### 3.1.2. Validation by the analytical model

To further validate the mechanical model in a whole SOFC cell plate, an analytical model developed by Hsueh [26] was applied in this section. In the analytical model, the stress distribution in the  $n$ th layer of a multi-layer can be calculated by considering the other  $n - 1$  layers to be a single, composite bar with composite material properties derived by averaging the material properties of each layer, weighted by layer thickness.

A multi-layer strip is shown schematically in Fig. 2, in which  $n$  layers of individual thicknesses,  $t_i$ , are laminated sequentially on a substrate with a thickness,  $t_s$ . The subscript  $i$  denotes the layer number from 1 to  $n$ .

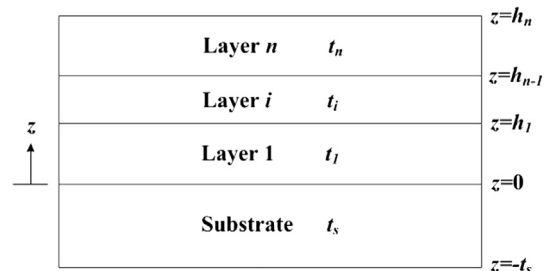
The relation between  $h_i$  and  $t_i$  is described by

$$h_i = \sum_{j=1}^i t_j \quad (i = 1 \text{ to } n) \quad (24)$$

The total strain in the system is formulated as

$$\varepsilon = c + \frac{z - t_b}{r} \quad (\text{for } -t_s \leq z \leq h_n) \quad (25)$$

where  $c$  is the uniform strain component given by (28),  $t_b$  dictates the location of the bending axis (29),  $r$  is the radius of curvature of the system (30). It should be noted that the bending axis in Hsueh model is defined as the line in the cross-section of the system where the bending strain is zero, which is different from the conventional neutral axis which is defined as the axis in the cross-section of the system where there are no longitudinal stresses or strains.

**Fig. 2.** Definition of the variables in analytical multi-layer thermal stress model.



$$c = \frac{\left(E_s t_s \alpha_s + \sum_{i=1}^n E_i t_i \alpha_i\right) \Delta T}{E_s t_s + \sum_{i=1}^n E_i t_i} \quad (26)$$

$$t_b = \frac{-E_s t_s^2 + \sum_{i=1}^n E_i t_i (2h_{i-1} + t_i)}{2 \left(E_s t_s + \sum_{i=1}^n E_i t_i\right)} \quad (27)$$

$$r = \frac{E_s t_s^2 (2t_s + 3t_b) + \sum_{i=1}^n E_i t_i [6h_{i-1}^2 + 6h_{i-1} t_i + 2t_i^2 - 3t_b (2h_{i-1} + t_i)]}{3 \left[E_s (c - \alpha_s \Delta T) t_s^2 - \sum_{i=1}^n E_i t_i (c - \alpha_i \Delta T) (2h_{i-1} + t_i)\right]} \quad (28)$$

The normal stresses in the layers are related to strains by

$$\sigma_i = E_i (\varepsilon - \alpha_i \Delta T) \quad (\text{for } i = 1 \text{ to } n, i = s) \quad (29)$$

If the system has a planar geometry rather than a strip, as is the case with the SOFC model the biaxial Young's modulus  $E'_i$  should be used instead of  $E_i$

$$E'_i = \frac{E_i}{1 - \nu_i} \quad (30)$$

where  $\nu$  is the Poisson's ratio.

The stresses were calculated for the ASSOFC and DSSOFC using both the analytical model and the mechanical model used in our study when it is free to bend under the application of a uniform temperature increase of 1000 K. In the analytical model, the anode is taken as the substrate layer, the electrolyte as layer 1 and the cathode as layer 2. The elastic properties are taken to be uniform and constant throughout a layer according to Table 6. The comparison of the two different solutions is shown in Fig. 3. The stress calculated by the model we used agrees well with the analytical result with a difference of less than 4%. The difference is due to the edge effects in the numerical model providing stress relief but the analytical model assumes the domain to be infinite in the in-plane dimension [29].

### 3.2. Stress comparison for DFFC configuration and common SOFC

The DFFC can be heated up to the working temperature within seconds [5], which is extremely fast compared to the heating time in common SOFC operating conditions. In this section, the stress distribution was simulated at different heat-up rates which

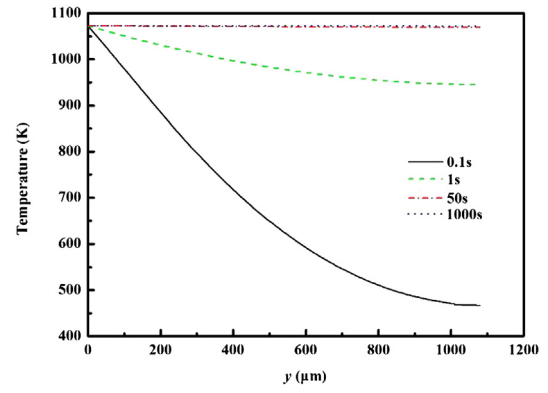


Fig. 4. Temperature distribution of three different heat-up rates.

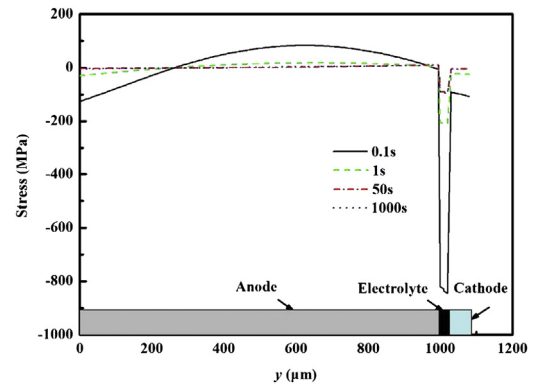


Fig. 5. Stress field distribution of DFFC with different heat-up rates.

represents the typical DFFC and the common SOFC operation. The heat-up time here means the time it takes the anode surface temperature to increase from room temperature (298 K) to operation temperature (1073 K). Since the SOFC is heated by the flame in DFFC condition, the heat-up time is the result of the rate of the homogeneous oxidation reaction and the thermal mass of the system. The homogeneous oxidation reaction is rather rapid with a characteristic time scale of several ms, and we considered this time scale should be the boundary limits (worst situation for DFFC operation) for the heat-up time of the anode gases. However, in practice, the heat-up time can also reach the time scale of several seconds ascribing to the heat transfer resistance, for instance, the convective heat transfer between the flame gas with the cell

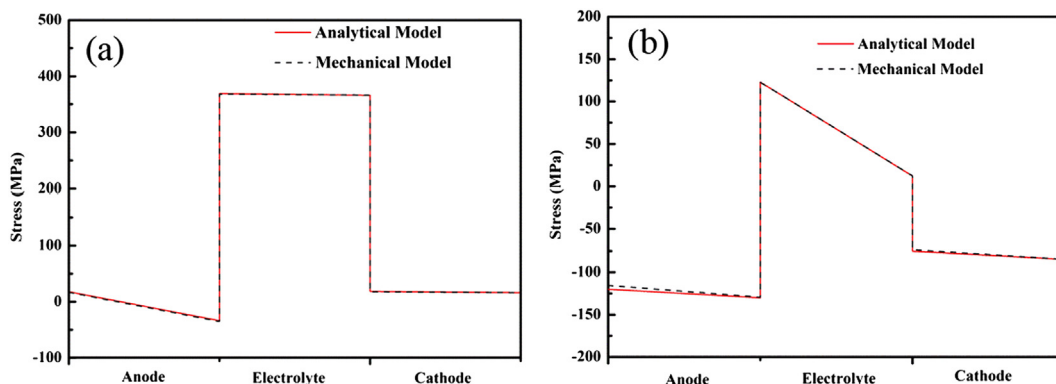


Fig. 3. Comparison of analytical solution with mechanical model analysis (a) ASSOFC (b) ESSOFC.

**Table 8**  
Fracture strength properties of each cell material [33].

	Anode (Ni/YSZ)	Electrolyte (YSZ)	Cathode (LSM)
Characteristic Strength (MPa)	79	154	75
Weibull modulus	7	8.6	3.7

surface. As a result, in our paper, four different heat-up rates (0.1 s, 1 s, 50 s and 1000 s from 298 K to 1073 K) were set as the temperature boundary conditions. The former three conditions represent the time scales for typical DFFC heat-up processes, which is referred as “DFFC case” in following text and the latter one represents the time scale for common SOFC heat-up processes is referred as “SOFC case” in following text. It should be noted that the anode-supported SOFC configuration is adopted in this section. The transient temperature distribution response and corresponding stress field when the anode temperature reaches 1073 K are shown in Fig. 4 and Fig. 5, respectively. In the DFFC case, when the anode temperature reaches 1073 K, the maximum transient temperature difference between the anode surface ( $y = 0$ ) and the cathode surface ( $y = 1150$ ) can even reach several hundred degrees (0.1 s and 1 s case); while the maximum transient temperature difference across the cell is only kept within  $1^\circ$  for the SOFC operating case. However, it should be noted that the temperature difference between the electrode surfaces in DFFC case can be controlled within several degrees when the heat-up rate is controlled to be relatively slow (about 1 min). Fig. 5 further shows several distinct features which can be easily identified. Firstly, the stress in the electrolyte and the cathode are always compressive while there are both compressive and tensile stresses in the anode. Secondly, both the maximum compressive stress across the three layers and the maximum tensile stress in the anode layer increase as the heat-up time decreases. The reason is that the temperature gradient through the fuel cell plate increases significantly when the heat-up time decreases, leading to greater thermal stress to the cell.

It is a well-known fact that the ceramic materials are susceptible to fracture under tensile stress and the compressive fracture strength of a ceramic material is normally much greater than its tensile fracture strength. The compressive stress in the cathode is kept in a low level so the cathode is usually unlikely to crack. The compressive stress within the electrolyte layer is much higher, which can even reach 800 MPa although the stress could be kept below the critical compressive fracture strength of 8YSZ which has been reported to be greater than 1 GPa [30]. Therefore, the anode layer which experiences the tensile stress is most susceptible to fracture in this situation.

The failure probability of the fuel cell can be calculated by Weibull statistics [31,32] as following:

$$P = 1 - \exp \left[ - \left( \frac{\sigma}{\sigma_0} \right)^m \right] \quad (31)$$

where  $\sigma_0$  and  $m$  are the characteristic strength and Weibull modulus, respectively. The fracture strength properties of the materials at operation temperature are summarized in Table 8.

**Table 9**  
Maximum tensile stress and failure probability of different heat-up rates.

	DFFC case			SOFC case
Heat-up time (s)	0.1	1	50	1000
$\sigma_{\max}$ in anode (MPa)	83	18	10.8	8.7
Failure probability	0.76	3.2E-05	8.9E-07	2.0E-07

The maximum tensile stress and failure probability are shown in Table 9. The rapid heat-up in DFFC operation may lead to large stress to the cell due to the temperature difference through the cell thickness. The corresponding failure probability shows four times of magnitude increase, from  $2.0\text{E-}07$  to  $8.9\text{E-}07$ , when the operation condition transfers from “SOFC case” to “DFFC case”, i.e. the heat-up time decreases from 1000 s to 50 s. And it shows two orders of magnitude increase when the heat-up time is 1 s. What's more, there exists another four orders of magnitude increase when the cell experiences a faster heat-up rate, which is 0.1 s from 298 K to 1073 K. As a conclusion, the rapid heat-up rate in DFFC case lead to larger thermal stress to the cell, thus increasing the failure probability. However, by controlling the heat-up rate at a relatively slow level, the increase of stress and failure probability can fall into an acceptable range.

### 3.3. Stress comparison for different fuel cell configurations

From the previous discussions, it can be seen that the cell in DFFC operation is more susceptible to fracture compared to the cell for being used in common SOFC operating condition due to its rapid heat-up rate. It is therefore valuable to choose an appropriate SOFC configuration which is more suitable for DFFC from the point of thermal shock resistance. In the present study, two different SOFC configurations, the ASSOFC and the ESSOFC, are compared. In the model, they get through the same heat-up process within 1 s from 298 K to 1073 K and the temporary temperature and stress are calculated when the anode reaches the operation temperature. The transient temperature distribution and stress distribution are shown in Figs. 6 and 7.

When the anode temperature reaches the usual SOFC operation temperature 1073 K, the transient temperature difference between the cathode and the anode is about 20 K in ESSOFC, which is much smaller than that in ASSOFC (more than 100 K). The reason is that the cell thickness of ESSOFC configuration is much smaller than that of ASSOFC and this contributes to the rapid heat conduction in the thickness direction and also helps to decrease the temperature difference between the cell layers. Despite of the smaller temperature difference, the maximum tensile stress in ESSOFC is greater than that in ASSOFC. And the cathode layer of ESSOFC undergoes a tensile stress which is different from the situation in ASSOFC, which means that the cathode of ESSOFC is more susceptible to fracture compared to ASSOFC. The failure probability calculation results of both cases are shown in Table 10. The failure probability of ESSOFC magnifies two orders compared to ASSOFC when undergoing a sudden heat-up process, which means that ASSOFC has better thermal shock resistance than ESSOFC thus is more suitable in DFFC operation.

### 3.4. Failure probability analysis for DFFC operation period

Except for the differences between operating conditions of DFFC and common SOFC due to the rather rapid heat-up rate, another significant difference is the operating environment including both the temperature and the composition. For example, the operating temperature of the common SOFC is well controlled by the electric furnace while the temperature of DFFC is mainly determined by the flame. In fact, the flame temperature and composition may vary significantly in a plane, such as the case of the flame provided by an ethanol lamp [2] or a Bunsen burner [1]. In this section the effect of flame non-uniformity on both the performance and the stress filed of the fuel cell is studied. The temperature distribution is supposed to follow the same trend as shown in Fig. 8. The degree of the non-uniformity is characterized by the various temperature difference

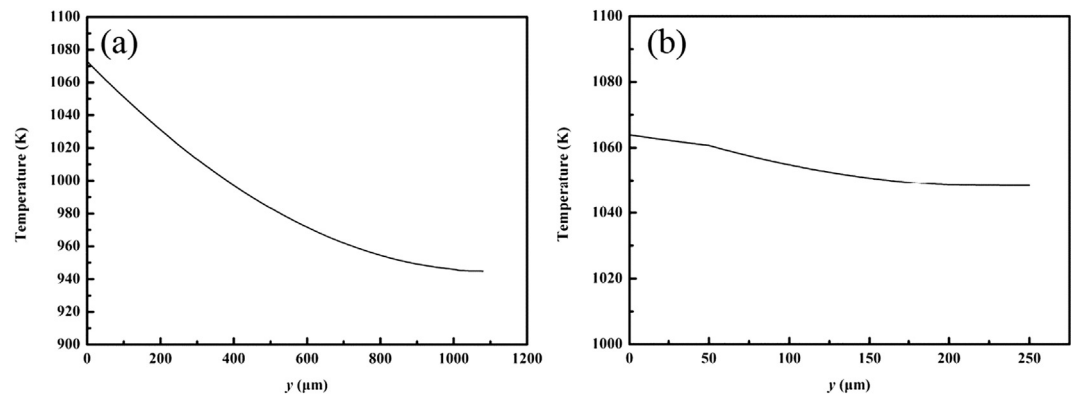


Fig. 6. Transient temperature distribution (a) ASSOFC (b) ESSOFC.

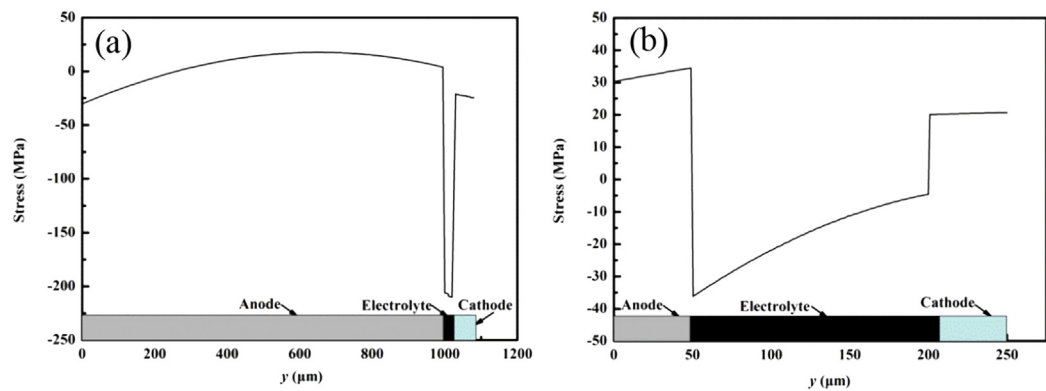


Fig. 7. Transient stress distribution (a) ASSOFC (b) ESSOFC.

Table 10  
Maximum tensile stress and failure probability for ASSOFC and ESSOFC.

	ASSOFC	ESSOFC	
	Anode	Anode	Cathode
$\sigma_{\max}$ (MPa)	18	35	20
Failure probability	3.2E-05	3.3E-03	7.5E-03

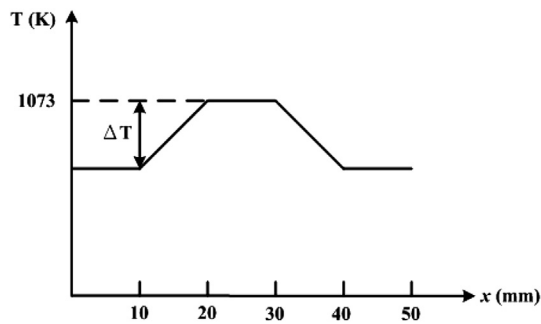


Fig. 8. Temperature distribution in x direction.

Table 11  
Equilibrium flame composition at  $\phi = 1.4$

H <sub>2</sub> (%)	H <sub>2</sub> O (%)	CO (%)	CO <sub>2</sub> (%)	N <sub>2</sub> (%)
6.0	17.5	7.5	4.8	64.2

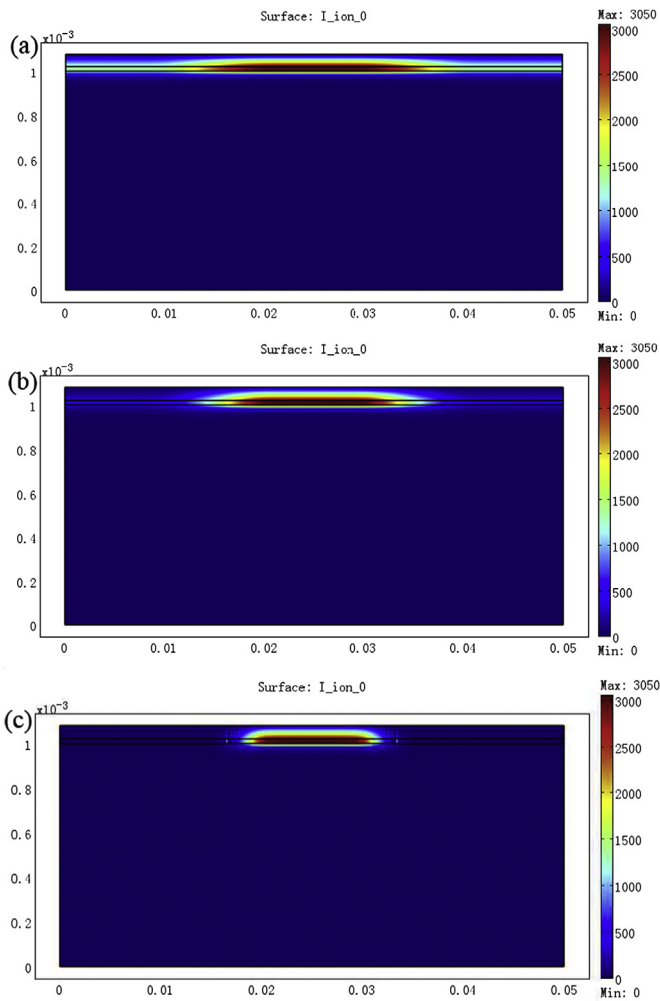
$\Delta T$ . The anode gas composition is set as the equilibrium flame composition at  $\phi = 1.4$ , as shown in Table 11.

Table 12 shows the maximum tensile stress and the corresponding failure probability of various  $\Delta T$  and Fig. 9 shows the ionic current density distribution of various  $\Delta T$  at a same voltage 0.7 V. The flame non-uniformity induces significant thermal stress to the fuel cell and increases the failure probability greatly. It should be noted that when the  $\Delta T$  reaches 750 K, i.e. the flame does not cover the whole fuel cell area, the failure probability reaches 1. It should be noted that the fuel cell performance is also greatly influenced by the flame temperature distribution, which is shown in Fig. 9. It can be seen that the ionic current density increases rapidly near the electrolyte, which means that the electrochemical reaction rate grows quickly near the electrolyte. Fig. 9 also indicates that the distribution of the current density is non-uniform, which is consistent with the uneven flame temperature distribution. The maximum ionic current density exists where the flame temperature reaches the highest and decreases rapidly in x direction as the temperature decreases. And the degree of the ionic current density non-uniformity is dependent on the flame temperature uneven degree.

Table 12  
Maximum tensile stress and failure probability of various  $\Delta T$

$\Delta T$ (K)	100	200	750
$\sigma_{\max}$ (MPa)	38	56	196
Failure probability	5.9E-03	8.6E-02	1





**Fig. 9.** Current density distribution of various  $\Delta T$  (a)  $\Delta T = 100$  K (b)  $\Delta T = 200$  K (c)  $\Delta T = 750$  K.

### 3.5. Failure probability analysis for DFFC start-up period

In the start-up period of DFFC, the fuel cell will not only get through a rapid heat-up process, the flame temperature can also be uneven. In this section, the heat-up rate is set to be 1 s from room temperature to operating temperature and the temperature difference  $\Delta T$  defined in Section 3.4 is set 100 K. The transient temperature and stress field are shown in Figs. 10 and 11. It can be seen

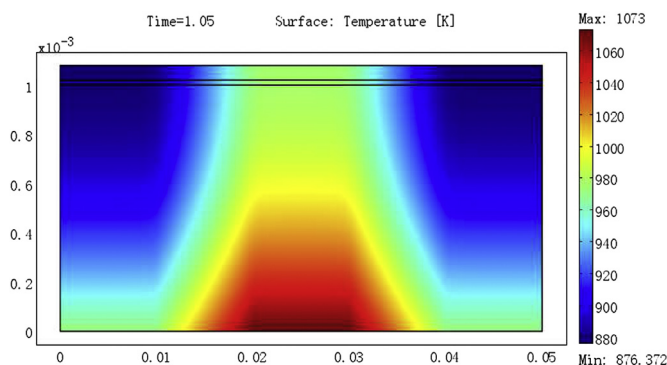


**Fig. 10.** Transient temperature field in the DFFC start-up period.

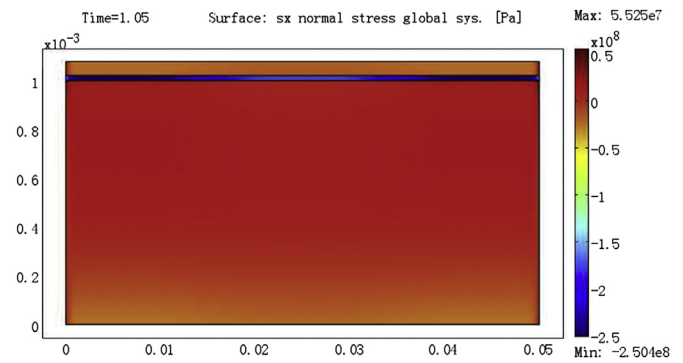


**Fig. 11.** Transient stress field in the DFFC start-up period.

that the transient temperature shows great non-uniformity in the fuel cell, in both the  $x$  and  $y$  directions, bringing huge stress to the cell. The failure probability reaches  $8E-02$ , which is much bigger than the situation that only one factor is taken into account (the rapid heat-up rate or the temperature non-uniformity). From the results above, we can come to a conclusion that the start-up period is the time when the cell is most likely to fracture, and the flame temperature uniformity is rather vital in DFFC operation, especially in the start-up period.

## 4. Conclusion

A detailed two-dimensional model of direct flame fuel cell was developed by considering the coupling effects of heterogeneous chemical and electrochemical reactions, electrode microstructure, transport processes of mass and charge, as well as the thermal mechanical stress. The stress distribution was simulated at different heat-up rates which represents the typical DFFC and the common SOFC operation. Both the ASSOFC and the ESSOFC are simulated under the same heat-up condition for DFFC. The failure probability for both the DFFC operation period and the start-up period was analyzed. The model is demonstrated to be a useful tool for understanding the mechanical stress distribution within DFFC cell and for the cell structure design and optimization. The results indicate that:

- (1) The rapid heat-up process which exists in DFFC operation brought in a great temperature gradient in the cell thickness direction, increasing the failure probability by 2–6 orders. But by controlling the heat-up rate at a relatively slow level (50 s from 298 K to 1073 K), the increase of stress and failure probability can fall into an acceptable range.
- (2) The failure probability caused by thermal shock of ESSOFC is about two orders higher than that of ASSOFC for DFFC operation. It suggests that ASSOFC would be better for being utilized in DFFC case in the aspect of thermal shock resistance.
- (3) The non-uniform flame temperature will not only induce more significant thermal stress, but also lead to serious non-uniform cell performance which may greatly increase the cell failure probability.
- (4) In the start-up period, the non-uniform temperature distribution of the cell due to the combined effects of the quickly rising of the temperature and the non-uniform flame temperature exists both in the cell thickness direction and the cell plane direction, further increasing the failure probability to around  $8E-02$ . This further indicates a flame which could provide a uniform temperature field is of great importance, especially during the start-up period.

## Acknowledgments

The authors acknowledge the Project 51106085 supported by National Natural Science Foundation of China and the Project 2014CB249201 supported by the National Basic Research Program of China (973 Program).

## References

- [1] M. Horiuchi, S. Sukanuma, M. Watanabe, J. Electrochem. Soc. 151 (2004) A1402–A1405.
- [2] K. Wang, R. Ran, Y. Hao, Z.P. Shao, W.Q. Jin, N.P. Xu, J. Power Sources 177 (2008) 33–39.
- [3] L.L. Sun, Y. Hao, C.M. Zhang, R. Ran, Z.P. Shao, Int. J. Hydrogen Energy 35 (2010) 7971–7981.
- [4] K. Wang, P.Y. Zeng, J. Ahn, Proc. Combust. Inst. 33 (2011) 3431–3437.
- [5] H. Kronemayer, D. Barzan, M. Horiuchi, S. Sukanuma, Y. Tokutake, C. Schulz, W.G. Bessler, J. Power Sources 166 (2007) 120–126.
- [6] M. Vogler, D. Barzan, H. Kronemayer, C. Schulz, M. Horiuchi, S. Sukanuma, Y. Tokutake, J. Warnatz, W.G. Bessler, ECS Trans. 7 (2007) 555–564.
- [7] J. Laurencin, G. Delette, F. Lefebvre-Joud, M. Dupeux, J. Eur. Ceram. Soc. 28 (2008) 1857–1869.
- [8] L.L.G. Kim, A. Chandra, J. Power Sources 195 (2010) 2310–2318.
- [9] A. Selimovic, J. Palsson, J. Power Sources 106 (2002) 76–82.
- [10] Y.X. Shi, N.S. Cai, C. Li, C. Bao, E. Croiset, J.Q. Qian, Q. Hu, S.R. Wang, J. Power Sources 172 (2007) 235–245.
- [11] Y.X. Shi, N.S. Cai, C. Li, C. Bao, E. Croiset, J.Q. Qian, Q. Hu, S.R. Wang, J. Power Sources 172 (2007) 246–252.
- [12] B.A. Haberman, J.B. Young, Int. J. Heat. Mass Transf. 47 (2004) 3617–3629.
- [13] A. Atkinson, A. Selcuk, Acta Mater. 47 (1999) 867–874.
- [14] P. Costamagna, P. Costa, V. Antonucci, Electrochim. Acta 43 (1998) 375–394.
- [15] S.H. Chan, Z.T. Xia, J. Electrochem. Soc. 148 (2001) A388–A394.
- [16] B. Todd, J.B. Young, J. Power Sources 110 (2002) 186–200.
- [17] Y.X. Shi, C. Li, N. Cai, J. Power Sources 196 (2011) 5526–5537.
- [18] D.L. Damm, Radiative and Transient Thermal Modeling of Solid Oxide Fuel Cells (Master thesis), Georgia Institute of Technology, USA, 2005.
- [19] B. Zitouni, G.M. Andreadis, B.M. Hocine, A. Hafsia, H. Djamel, Z. Mostefa, Int. J. Hydrogen Energy 36 (2011) 4228–4235.
- [20] S. Giraud, J. Canel, J. Eur. Ceram. Soc. 28 (2008) 77–83.
- [21] A. Selcuk, A. Atkinson, J. Eur. Ceram. Soc. 17 (1997) 1523–1532.
- [22] A. Atkinson, T.M.G.M. Ramos, Solid State Ionics 129 (2000) 259–269.
- [23] H. Hayashi, T. Saitou, N. Maruyama, H. Inaba, K. Kawamura, M. Mori, Solid State Ionics 176 (2005) 613–619.
- [24] Y.H. Du, N.M. Sammes, G.A. Tompsett, D.L. Zhang, J. Swan, M. Bowden, J. Electrochem. Soc. 150 (2003) 74–78.
- [25] Y.X. Shi, H.J. Wang, N.S. Cai, J. Power Sources 208 (2012) 24–34.
- [26] C.H. Hsueh, Thin Solid Films 418 (2002) 182–188.
- [27] E. Lara-Curzio, Durability and Reliability of Solid Oxide Fuel Cells Solid State Energy Conversion Alliance (SECA), Core Technology Peer Review Workshop, Tampa, FL (US), 01/27/2005–01/28/2005.
- [28] W. Fischer, J. Malzbender, G. Blass, R.W. Steinbrech, J. Power Sources 150 (2005) 73–77.
- [29] R. Clague, A.J. Marquis, N.P. Brandon, J. Power Sources 210 (2012) 224–232.
- [30] T. Kato, N.S. Wang, A. Negishi, A. Momma, Y. Kasuga, K. Nozaki, in: Proceedings of the Third International Fuel Cell Conference, Nagoya, November 3, 1999, p. 461.
- [31] T. Zhang, Q. Zhu, W.L. Huang, Z. Xie, X. Xin, J. Power Sources 182 (2008) 540–545.
- [32] G. Anandakumar, N. Li, A. Verma, P. Singh, J. Kim, J. Power Sources 195 (2010) 6659–6670.
- [33] A. Nakajo, Z. Willemin, J.V. Herle, D. Favrat, J. Power Sources 193 (2009) 203–215.